nature communications

Article

https://doi.org/10.1038/s41467-026-69993-x

Decoding local framework dynamics in the ultra-small pore MOF MIL-120(Al) CO_2 adsorbent using machine-learning potential

Received: 3 September 2025

Accepted: 11 February 2026

Published online: 26 February 2026

Check for updates

Dong Fan[1,2], Felipe Lopes Oliveira[2], Satyanarayana Bonakala[2], Mohammad Wahiduzzaman[2] & Guillaume Maurin[2,3]

Metal–organic frameworks (MOFs) with ultra-small pores offer an optimal environment to effectively capture guest molecules such as CO_2. Subtle local dynamics of their frameworks, either throughout reorientation of functional groups grafted to the organic linkers or those present in their inorganic nodes, is expected to play a major role in their sorption behaviours. Herein, we investigated the local dynamics of bridging hydroxyl group (μ_2-OH) in the ultra-small pore MOF MIL-120(Al) using DFT combined with a purpose-trained machine-learning potential (MLP). Six distinct μ_2-OH configurations were identified with low interconversion barriers (0.07–0.19 eV), indicating significant dynamic behaviour at room temperature. Grand canonical Monte Carlo and hybrid GCMC–MD simulations driven by the MLP demonstrate that adsorption isotherms and low-pressure behaviour are sensitive to μ_2-OH ordering and whether framework and cell relaxation are considered. While standard rigid force-field simulations overestimated the heat of adsorption, MLP-driven GCMC-MD simulations successfully captured framework relaxation and dynamic μ_2-OH reorientation under CO_2 loading. This work establishes that a reliable description of the local structure, such as reorientation/flipping of bridging hydroxyl groups, is a key feature to gain an accurate description of the guest locations and energetics in ultra-small pore MOFs.

Metal–organic frameworks (MOFs) are crystalline coordination polymers constructed from metal ions or clusters connected by organic linkers, forming highly ordered nanoporous structures[1–6]. Owing to the unique tunability of their pore size, shape and chemical functionality, MOFs have emerged as promising materials for diverse applications including CO_2 capture[7–12]. In particular, MOFs with ultra-small pores/channels combined potentially with polar groups decorating the pore walls offer a unique confined environment to favor an effective packing of CO_2 in their pores[13]. This confers to this sub-class of MOFs attractive CO_2 sorption performance even in the presence of co-adsorbed species such as N_2 or CH_4 of key importance in the context of CO_2 capture in post- and pre-combustion conditions[14–17]. Notably, it has been documented that a very tiny change of the pore size of isoreticular ultra-small pore MOFs by modulating the nature of the metal sites as for example in the KAUST-8 series (Al, Fe, Ga) can fine-tune their CO_2 sorption properties[18–20]. Local flexibility of such a sub-class of MOFs that can arise either from the dynamics of the functional groups of the organic linkers or the orientation of chemical functions present in the inorganic nodes can also play a key role in the CO_2 sorption mechanism[15,21,22]. This structural dynamics is often overlooked, although decisive in controlling the CO_2/MOF interactions by modulating slightly the MOF pore confinement. This is especially true for ultra-small pore MOFs containing bridging hydroxyl functions, namely, μ_2-OH groups, with a notable experimental limitation lying in

[1]School of Materials Science and Engineering, Chongqing Jiaotong University, Chongqing, PR China. [2]ICGM, Univ. Montpellier, CNRS, ENSCM, Montpellier, France. [3]Institut Universitaire de France, Paris, France. e-mail: guillaume.maurin1@umontpellier.fr

determining hydrogen atom positions since H atoms scatter X-rays only weakly and their locations cannot be detected by X-ray diffraction technique. As a result, hydrogen atoms are typically added post hoc based on standard bond lengths and geometries criteria[23]. Such empirical treatments assume that μ_2-OH orientations exert only a minor influence on MOF framework properties, which might be only valid for medium- to large-pore MOFs. MIL-120(Al), first reported in 2009 by Férey and co-workers, is one representative ultra-small pore MOF[24]. This aluminum MOF is built from the assembly of tetratopic linker 1,2,4,5-benzenetetracarboxylate and infinite chains of edge-sharing AlO_6 octahedra[24] forming a three-dimensional network with one-dimensional ultra-small pores (~ 5.4 × 4.7 Å) aligned along the *c*-axis. This sustainable, easily scaled-up and low-cost MOF combines excellent thermal and hydrolytic stability with CO_2 adsorption performance as attractive as the best MOFs reported so far for CO_2 capture under flue-gas conditions (see Supplementary Table 1). This makes this MOF a promising candidate for further integration into large-scale industrial processes[25,26]. Our preliminary findings suggested that the orientation of the μ_2-OH groups present in this MOF affects the CO_2 location in the pores and their associated energetics[25]. Nevertheless, a systematic exploration of the role played by the local dynamics of these μ_2-OH groups on the CO_2 sorption properties of MIL-120(Al) and beyond other related-MOFs, is yet to be realized.

To address this gap, the present work employs a combination of DFT calculations and a MLP approach to systematically map the configurational landscape of μ_2-OH groups in MIL-120(Al). By quantifying the electronic stability of representative configurations, their structure interconversion pathways and their impact on CO_2 adsorption thermodynamics, this study uncovers a previously overlooked structural degree of freedom in MIL-120(Al), and establishes a transferable computational framework to capture the impact of functional groups orientations on MOFs properties more broadly.

Results

Exploration of the local structural features of MIL-120(Al)

The structure of MIL-120(Al) comprises edge-sharing AlO_6 octahedra linked by bridging hydroxyl (μ_2-OH) groups forming one-dimensional chain motifs (cf. Fig. 1a). Among several possible μ_2-OH groups orientations, we constructed six representative structure models of MIL-120(Al) that differ exclusively in the orientation of the four μ_2-OH groups present in the unit cell, namely MIL-120(Al)-A, MIL-120(Al)-B, MIL-120(Al)-C, MIL-120(Al)-D, MIL-120(Al)-E and MIL-120(Al)-F (cf. Fig. 1b) while the MOF skeleton remains the same as shown in Fig. 1c with identical simulated X-ray diffraction patterns for all structure models in line with the corresponding experimental data[25]. Notably, because X-ray diffraction cannot resolve the positions of hydrogen atoms, previous studies have adopted MIL-120(Al)-F as a single representative structure model[24,25]. DFT geometry optimizations with full relaxation of atomic positions and cell parameters for the six structure models revealed clear differences in total electronic energy. MIL-120(Al)-A is the most stable configuration, while MIL-120(Al)-F has the highest energy, with a energy difference of ~0.59 eV per unit cell. Interestingly, the MIL-120(Al)-F configuration, reported in the literature for this MOF[24], corresponds to a μ_2-OH group orientation that is not energetically favorable. In the lowest-energy MIL-120(Al)-A configuration, the μ_2-OH groups form an interlocking hydrogen-bond

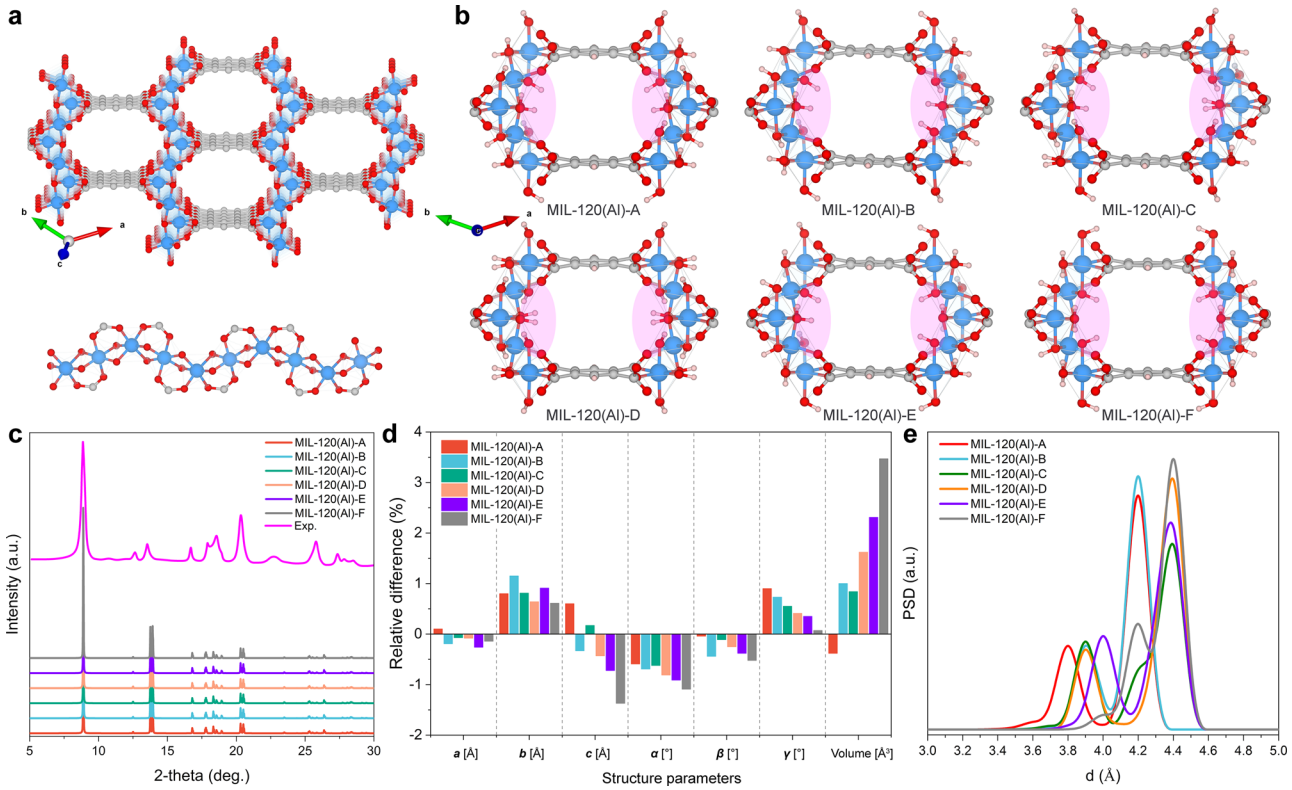

Fig. 1 | The rich structure landscape of MIL-120(Al). a The crystal structure of MIL-120(Al) viewed along [001] direction highlighting the ultra-small 1D channel (top). Inorganic building blocks of the *trans-cis* edge-sharing $Al(OH)_4O_2$ octahedra along the direction of the MOF channel (bottom). H atoms were excluded for clarity. **b** Representation of the DFT-optimized structure models for the six variants of MIL-120(Al) with the different orientations of the μ_2-OH groups pointing towards the channel. The shadow area highlights the differences between the variants. Color code used in the structure models: Al, blue; O, red; C, gray; H, pink. **c** A comparison of the X-ray diffraction patterns for the DFT-optimized MIL-120(Al) configurations and the corresponding experimental data. **d** The percentage difference observed in the lattice parameters for the six MIL-120(Al) structures relative to the experimental values[25]. **e** Computed pore size distributions (PSD) for the different DFT-optimized MIL-120(Al)s.

network linking adjacent $Al(OH)_4O_2$ octahedral chains, as shown in Supplementary Fig. 1. The μ_2-OH groups orientate towards the neighboring $Al(OH)_4O_2$ chain on one side, establishing directional hydrogen bonds formed between the hydroxyl hydrogen atom of the μ_2-OH groups and the nearby Al–O framework oxygen of the adjacent polyhedral chains, while on the opposite side, they are pointing towards the channel. This cooperatively interlocking motif stabilizes the MIL-120(Al)-A configuration. In contrast, the other five variants lack such motif, with more disordered μ_2-OH orientations that result in weaker cooperative intramolecular hydrogen-bond interactions. These six structure models exhibit only minor variations in their lattice parameters: the relative changes in ***a***, ***b***, ***c***, α, β and γ remain within ±1.4%, and the cell volumes within ±3.5%, as shown in Fig. 1d and Supplementary Table 2. Despite these similar crystallographic features, their pore size distributions (PSDs) deviate with the main peak contribution distributed between ~3.8 and 4.2 Å, depending on the orientations of the μ_2-OH groups towards the MOF channel (cf. Fig. 1e). Owing to the ultra-small pores of this 1D MOF channel, such sub-angstrom fluctuations in aperture can markedly impact guest accessibility and modulate MOF/guest interactions. Therefore μ_2-OH orientation represents a 'hidden' structural degree of freedom not detectable by standard X-ray diffraction techniques yet capable of influencing functional pore dimensions and energetics.

Machine-learning potential development and exploration of the stability of the different MIL-120(Al) configurations

To efficiently probe the full configurational ensemble and to enable in-depth exploration of the possible structure interconversion pathways between all these structure models, we developed a robust MLP, trained on a comprehensive MIL-120(Al)-specific DFT dataset, as shown in Supplementary Fig. 2. The dataset includes a wide range of DFT-optimized MOF structures, static single-point DFT calculations, MOF structures loaded with different CO_2 uptakes, intermediate/transition structures obtained via climbing-image nudged elastic band (CI-NEB)[27], and Ab Initio Molecular Dynamics (AIMD) snapshots under diverse NVT/NPT conditions (details of the collection, training, validation, and testing of the entire dataset can be found in Supplementary Note 1 and Supplementary Figs. 3, 4). We then trained a DeePMD potential[28] and evaluated its coverage with the t-distributed stochastic neighbor embedding (t-SNE) method. As shown in Fig. 2a, distinct datasets occupy different regions of the descriptor space, allowing for a clear view of the occupation of each component in the entire dataset. This plot enables to confirm that there is an effective sampling of the configurational space throughout the MLP training. Figure 2b shows a comparison between the MLP-and DFT-derived energies for the empty and CO_2-loaded (one CO_2 per unit-cell, ~2.02 mmol g^{-1}) MIL-120(Al) structures with root mean square error (RMSE) values of 0.217 meV atom-1 and 0.268 meV atom-1 (cf. Supplementary Table 3), respectively. Notably, these deviations are significantly lower than the values generally obtained for a standard MLP[29,30], demonstrating the high accuracy and effectiveness of the MLP training process. The energy–volume curves derived from DFT optimization, MLP single-point evaluation based on DFT-optimized geometries, and fully MLP-relaxed structures show very good agreement, as shown in Fig. 2c in terms of both minima and overall curvatures of the plot. Phonon spectra predicted by MLP also show no imaginary modes at the whole Brillouin-zone path for all MIL-120(Al) variations, confirming the dynamical stability of all these configurations (cf. Fig. 2d). These results demonstrate that the trained MLP achieves near-DFT-level accuracy in describing the energetics, vibrational properties, and optimized geometries across the MIL-120(Al) configurations.

We then assessed the elasticity and failure responses of all six MIL-120(Al) variants by calculating the linear compressibility, Young's modulus, shear modulus, and Poisson's ratio (see Fig. 2e and Supplementary Table 4). These calculations revealed that local μ_2-OH ordering systematically affects the directional mechanical properties of MIL-120(Al). MIL-120(Al)-A in which μ_2-OH groups form cooperative *inter-chain* hydrogen bonding, exhibits stiffer coupling and reduced compressibility perpendicular to the chain axis. In contrast, variants with more disordered or pore-facing OH orientations (e.g. MIL-120(Al)-B and MIL-120(Al)-F) demonstrate softer inter-chain contacts and significantly higher compressibility in these directions. This is quantified by the maximum-to-minimum compressibility ratio, which reaches 3.6 for MIL-120(Al)-B in line with a substantial mechanical heterogeneity driven by the μ_2-OH groups arrangement.

Calculated stress-strain curves further confirm that μ_2-OH orientation controls failure behavior. The chain direction ([010]) is the stiffest and most ductile axis in all variants, due to the rigid AlO_6 octahedral backbone. Consequently, ultimate tensile strains along [100] exceed 50% across the series. However, the detailed shape of the stress–strain curve and the onset of strain softening vary systematically with μ_2-OH groups ordering (cf. Supplementary Figs. 5–8). This mechanical behavior originates from the anisotropic topology of the 1D rigid AlO_6 octahedra chains coupled with flexible hydrogen-bonded interchain contacts. Therefore, although the six MOF configurations exhibit comparable volumetric averages of the elastic modulus, their anisotropic mechanical responses differ significantly.

Structure interconversions and associated local μ_2-OH reorientations between MIL-120(Al) configurations predicted by DFT and MLP calculations

Quantitative characterization of the kinetics of μ_2-OH orientations is essential for determining whether the identified polymorphs correspond to kinetically trapped states or whether they remain dynamically accessible under experimental conditions. For this purpose, we calculated the minimum-energy pathways between the different polymorphic states of MIL-120(Al)s using the climbing image nudged elastic band (CI-NEB) method[27,31] interfaced with the DFT and MLP levels of theory. Representative CI-NEB profiles obtained from DFT (Fig. 3a) and MLP (Fig. 3b) revealed relatively moderate energy barriers of 0.07–0.19 eV per unit cell for the interconversion between the empty configurations. Importantly, the MLP-predicted pathways quantitatively reproduced the DFT-derived energy barriers and transition-state geometries across all computed systems. The energy profiles and the intermediate images are highly consistent, with almost complete overlap observed between the MLP and DFT curves (cf. Supplementary Figs. 9–26 for the complete curves). This quantitative agreement is particularly notable because CI-NEB probes transition-state regions of the potential-energy surface, where interpolation errors often compromise the accuracy of predicted energy. Thus, the MLP performance confirms that the training set adequately sampled both equilibrium configurations and critical transition configurations.

The presence of CO_2 in the MOF pores is shown to only slightly affect these energy barriers. For some pathways, CO_2 marginally reduces the energy barrier (~ 3–8%), indicating that guest-mediated stabilization of specific transition states occurs through directional host–guest interactions. Analysis of CI-NEB snapshots for the empty MIL-120(Al) structures (Fig. 3c) shows that the structure interconversions imply a dynamic reorientation of the μ_2-OH groups, the H-atom temporarily forming and breaking hydrogen bonds with neighboring oxygens, primarily with the carboxylate oxygens of the pyromellitate linker, while maintaining its covalent bond with the original μ_2-O. A synchronous H-atom displacement and transient hydrogen-bond rearrangement account for the relatively moderate energy barriers involved, highlighting the high degree of freedom of this μ_2-OH group

https://doi.org/10.1038/s41467-026-69993-x

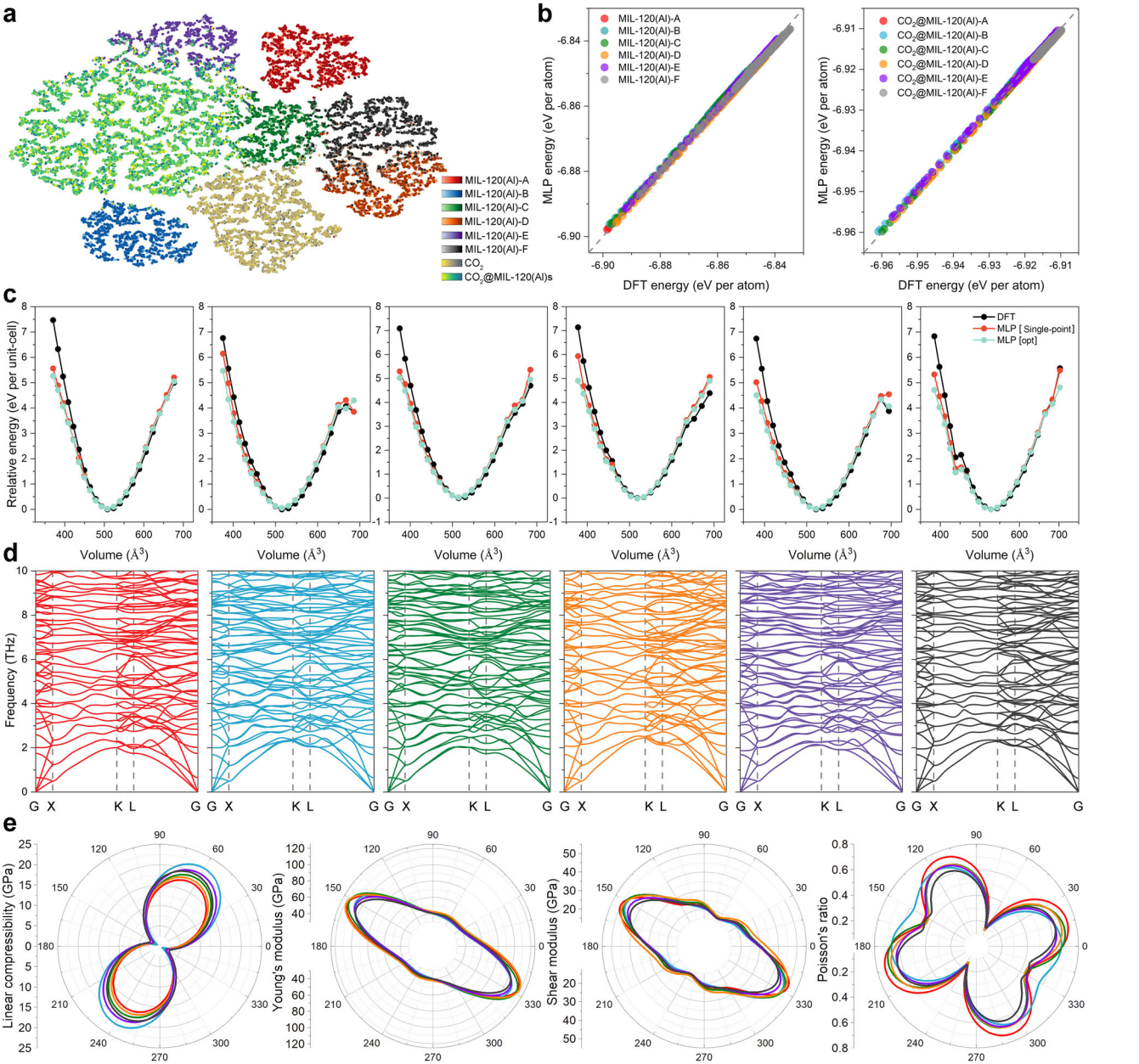

Fig. 2 | Structural stability and mechanical properties of MIL-120(Al) configurations predicted by MLP against DFT calculations. a t-SNE embedding of the training dataset shows distinct sampling of the CO_2 molecules, MIL-120(Al) structure variants, and corresponding adsorbed states. Points were colored according to their corresponding structural types. **b** Linear relationship plots of MLP against DFT energies for the empty MIL-120(Al) (left) and CO_2-loaded MIL-120(Al) configurations (right). **c** Energy–volume curves computed by DFT and MLP (including single-point calculations and MLP-based relaxation) calculations for the six different MIL-120(Al) configurations. **d** MLP-predicted phonon spectra of the different MIL-120(Al) configurations. MIL-120(Al)-A to MIL-120(Al)-F are arranged from left to right in sequence. **e** Polar coordinate diagrams of the mechanical properties of the different MIL-120(Al) configurations derived from elastic constants (along the *ab* plane). The averaged mechanical properties of all MIL-120(Al) configurations can be found in Supplementary Table 4.

and how it can easily reorient, thereby affecting the features of the accessible MOF pores.

In-depth microscopic understanding of CO_2 adsorption in MIL-120(Al)s by DFT and MLP calculations

Next, we assessed how spatial distribution of μ_2-OH groups in MIL-120(Al)s modulates the adsorption geometries and energetics of CO_2 within the MOF channels. To avoid bias towards local minima, the adsorption site locator protocol employed a random insertion approach, followed by MLP-based relaxation and subsequent DFT refinement of the lowest-energy candidates. MLP- (Fig. 4a) and DFT- (Supplementary Fig. 27)-optimized geometries for the six MOF variants loaded by 1 CO_2 molecule per unit cell, show extremely similar guest locations and orientations, confirming that the MLP captures the local host–guest interactions accurately. Detailed analysis of the adsorbed CO_2 orientations uncovers a direct correlation with the μ_2-OH group arrangement. In most cases, the CO_2 molecular axis is aligned nearly perpendicular to the pore axis. This maximizes directional interactions with μ_2-OH groups pointing towards the channel. Both our DFT- and MLP-optimized geometries show that the O(CO_2)···H(μ_2-OH) separating distances are in the range of 2.17 ~ 2.74 Å, with both MLP and DFT optimized geometries giving consistent distances and geometries (cf. Fig. 4a). By contrast, in MIL-120(Al)-C and MIL-120(Al)-D, the local μ_2-OH distribution differs: the bridging

https://doi.org/10.1038/s41467-026-69993-x

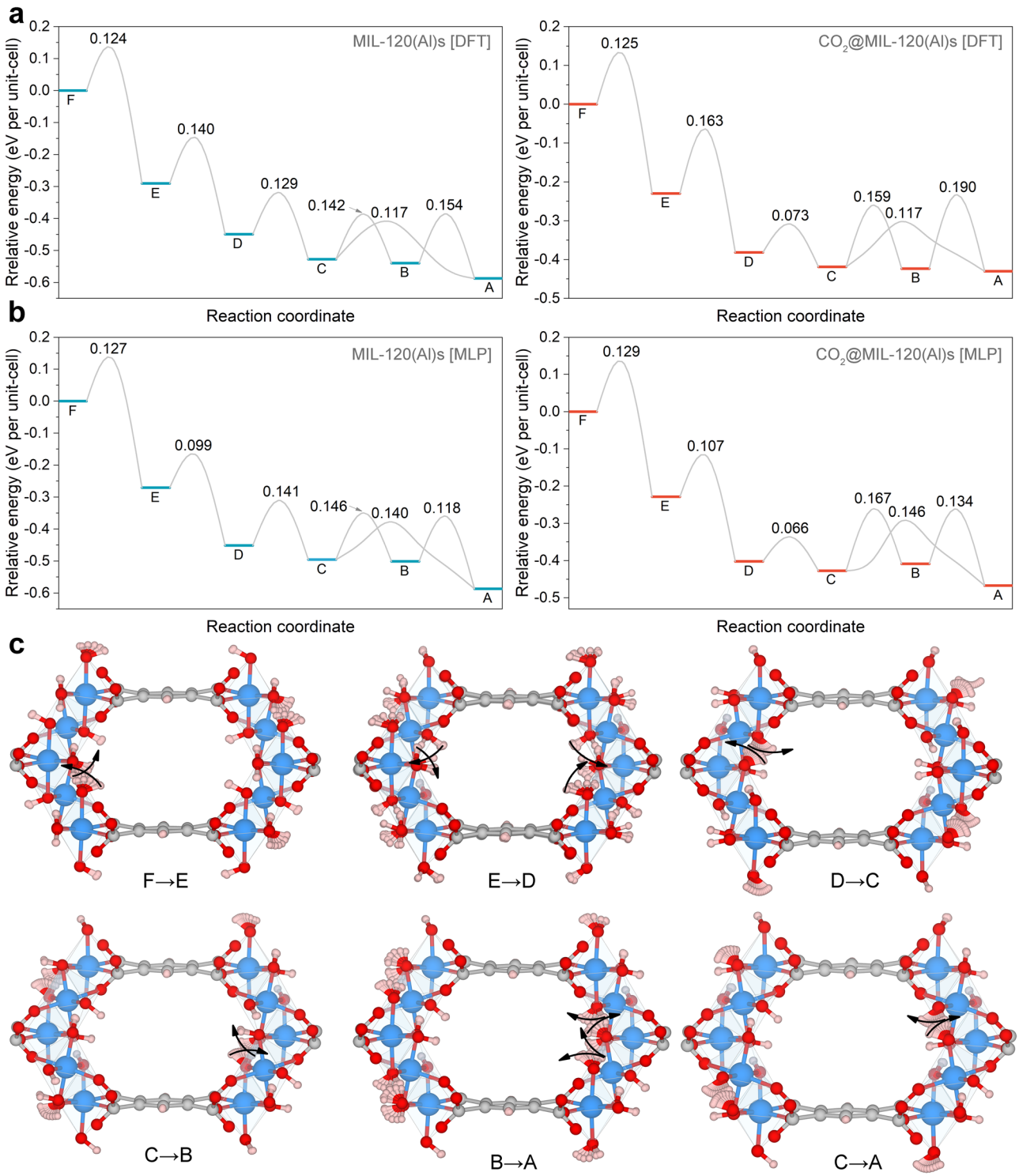

Fig. 3 | Structure interconversion and associated μ_2-OH reorientation pathways of MIL-120(Al)s predicted by DFT- and MLP-CI-NEB calculations. **a** Representative CI-NEB profiles (in eV unit) for the empty (left) and CO_2-loaded (right) MIL-120(Al) structures using the DFT-CI-NEB approach. **b** Corresponding energy profiles using MLP-driven calculations that closely reproduce DFT barriers. **c** Structural snapshots and H atom trajectories illustrating μ_2-OH reorientations for six representative transition paths indicated in the figure. The black arrows indicate the directions in which the μ_2-OH orientation changes. Color code: Al, blue; O, red; C, gray; H, pink.

hydroxyl groups adopt orientations more axial to the channel, which in turn sterically favor a parallel CO_2 alignment along the channel. Notably, the presence of CO_2 produces only minor adjustments of μ_2-OH orientations relative to the empty frameworks, consistent with the earlier finding that CO_2 does not substantially alter the structure interconversion energy barriers.

In terms of CO_2 interaction energy at 0 K, the MLP predictions deviate from DFT by at most 2.3 kJ mol^{-1} across all examined configurations (cf. Fig. 4b). Interestingly, our MLP performs better than other universal MLPs reported in the literature, such as MACE-MP-0 and fine-tuned MACE-DAC models[32,33] leading to a systematic over- and under-estimation of the interaction energies, respectively (Fig. 4b). This

https://doi.org/10.1038/s41467-026-69993-x

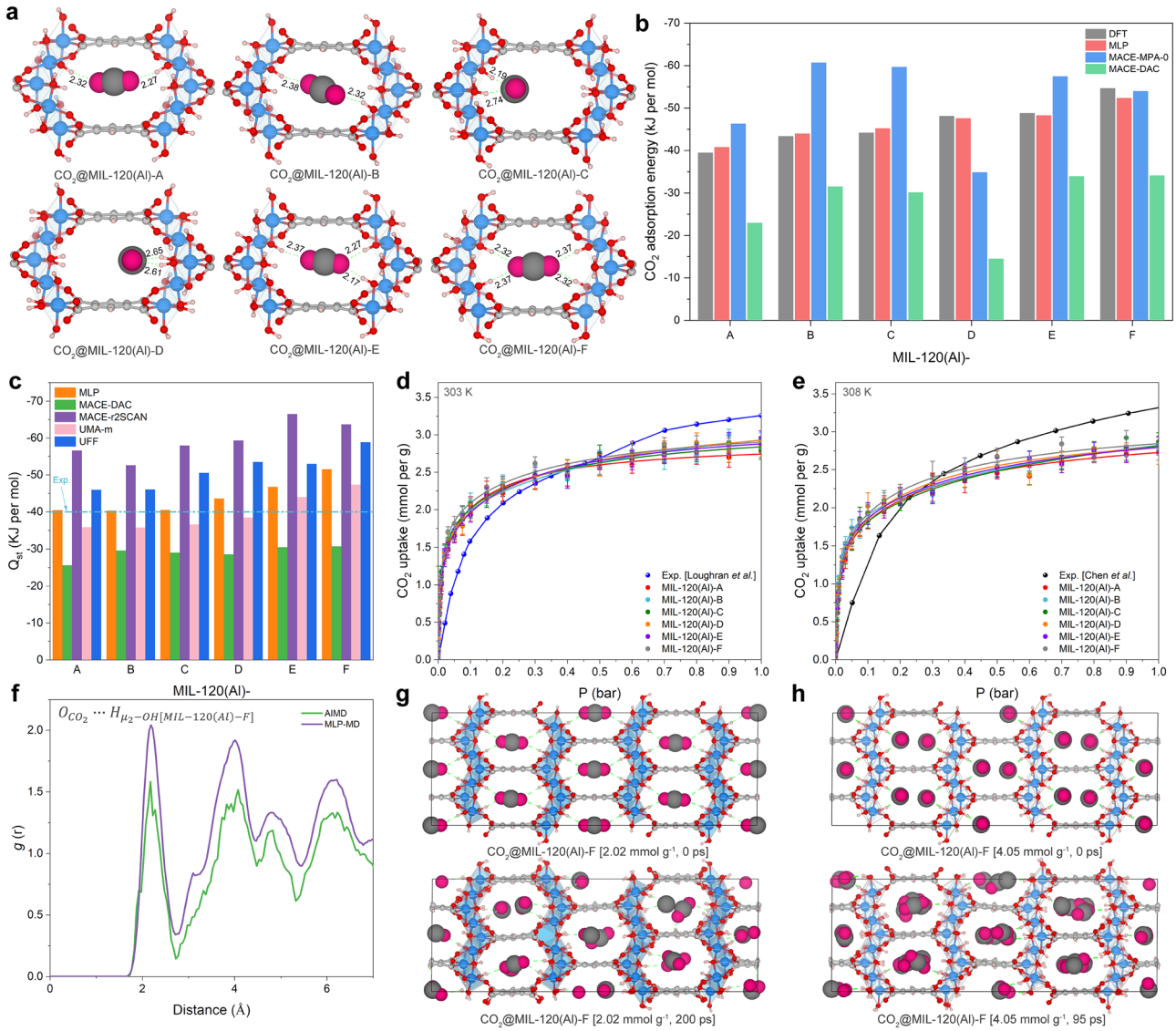

Fig. 4 | In-depth microscopic understanding of the CO_2 adsorption in the diverse MIL-120(Al) configurations. a MLP-derived lowest-energy CO_2 adsorption sites in the different MIL-120(Al) structures for a loading of 1 molecule of CO_2 per unit cell (~2.02 mmol g^{-1} at 298 K). The corresponding data for a loading of 2 molecules of CO_2 per unit cell (4.05 mmol g^{-1} corresponding to the experimental uptake at 1 bar) are shown in Supplementary Fig. 29. The green dashed line represents the shortest distance between CO_2 and the μ_2-OH groups of MIL-120(Al) (unit: Å). **b** CO_2 interaction energies computed by DFT, our MLP model, and other MLPs including MACE-MPA-0 and MACE-DAC[32,33], respectively. These interaction energies (E_{int}) were computed as $E_{int} = E_{CO_2@MOF} - (E_{MOF} + E_{CO_2})$ using the optimized CO_2 molecule, the optimized empty MIL-120(Al)s, and the optimized CO_2@MIL-120(Al)s at each theoretical level (MLP/DFT). **c** Widom-insertion derived isosteric heats (Q_{st}) at 298.15 K using our MLP, universal MLPs (including MACE-DAC[33], MACE-r^{2}SCAN[34], UMA-m[35]), and classical UFF[36] force field, respectively. The dashed line represents the experimental Q_{st} value reported earlier[25]. GCMC simulated adsorption isotherms for CO_2 in MIL-120(Al)s at **d** 303 and **e** 308 K using MLP-based GCMC-MD (NPT) approach, respectively. Error bars represent the standard deviation calculated over the equilibrated part of the simulation. We collected the experimental data from two different literature sources for comparison[25,26]. **f** Radial distribution functions (RDF) for $O_{CO_2} \cdots H_{\mu_2-OH[MIL-120(Al)-F]}$ atom pairs at 300 K computed via AIMD and MLP-MD approaches both in the NVT ensemble for a CO_2 loading of 2.02 mmol g^{-1}. **g** Representative MLP-MD snapshots for MIL-120-F loaded with 2.02 mmol g^{-1} of CO_2, showing configurations at 0 ps (top) and 200 ps (bottom). **h** Representative MLP-MD snapshots for MIL-120-F loaded with 4.05 mmol g^{-1} of CO_2, showing configurations at 0 ps (top) and 95 ps (bottom). The snapshots illustrate the rapid reorientation of pore-exposed μ_2–OH groups and the consequent reorganization of adsorbed CO_2 molecules. Color code for snapshots: Al, blue; O, red; C, gray; H, pink; CO_2, black and magenta for C and O respectively.

strongly suggests that universal MLPs are poorly suited for MOFs with polar functionalities and local structural flexibility, especially when μ_2-OH group dynamics dominate host–guest interactions. Furthermore, the Widom insertion calculations performed using our trained MLP led to isosteric heats (Q_{st}) which closely match the experimental values for MIL-120(Al)-A, MIL-120(Al)-B and MIL-120(Al)-C, as shown in Fig. 4c, compared to typical universal MLPs that show substantial deviations. Overall, the highest Q_{st} value is obtained for MIL-120(Al)-F, in line with a more confined pore environment of this configuration characterized by the highly ordered orientation of μ_2-OH groups towards the pore channels. The use of UFF leads to a substantial overestimation of Q_{st} for all configurations as compared to the corresponding experimental data supporting the need for an empirical tuning of the force-field parameters to obtain a better agreement with experimental data (Supplementary Fig. 28).

The small interconversion energy barriers between the different MIL-120(Al) structure models suggest that CO_2 adsorption can readily trigger structural transitions. Each MIL-120(Al) configuration is therefore expected to contribute individually to the experimentally observed CO_2 uptake across the full pressure range. However,

conventional GCMC approaches typically treat the MOF framework as rigid and rely on empirical force fields such as UFF[36]. Such simulations cannot capture local, dynamical rearrangements of framework motifs, e.g. μ_2-OH reorientations, that we demonstrated to be important in the ultra-small-pore MIL-120(Al). Moreover, the UFF parametrization is poorly suited to describe the interactions between highly polar and sterically constrained environments with guest molecules as shown in Supplementary Fig. 30 with a deviation between the corresponding GCMC simulated adsorption isotherms for all configurations and the experimental data. Taken together, these effects lead to a systematic overestimation of the simulated Q_{st} and CO_2 adsorption uptake compared to experimental data as already reported for such families of MOFs[25,37,38]. Empirical reparameterization of UFF can be used to align with specific experiments (see Supplementary Figs. 31–33), however this approach lacks transferability and predictive ability. To evaluate the impact of the μ_2-OH orientation associated with these distinct configurations on the overall CO_2 sorption isotherms, we performed MLP-based GCMC simulations using three distinct approaches (cf. Supplementary Figs. 34–51): (1) fully rigid MIL-120(Al) framework, where both atomic positions and unit cell were fixed, (2) hybrid GCMC-(NVT) MD scheme, coupling MC steps with molecular dynamics (MD) steps in the NVT ensemble (relaxed atomic positions, fixed unit cell parameter), and (3) hybrid GCMC- (NPT) MD scheme coupling MC steps with MD steps in the NPT ensemble (full relaxation of both atomic positions and unit cell parameters). The rigid-framework MLP-GCMC simulations were found to describe the experimental isotherm in the low-pressure region more faithfully than UFF-GCMC simulations as shown in Supplementary Fig. 52. The MLP-GCMC-(NPT) MD calculations performed starting with the different structure models converge towards similar adsorption isotherms closely matching those obtained by MLP-GCMC-(NVT) MD calculations for the MIL-120(Al)-A to MIL-120(Al)-D models (cf. Supplementary Fig. 53). This observation is consistent with the relative low energy between all these structures models, suggesting a structure relaxation towards the most stable MIL-120(Al) structures, i.e. MIL-120(Al)-A to MIL-120(Al)-D (cf. Fig. 3) upon adsorption. The MLP-based GCMC–(NPT) adsorption isotherms (Fig. 4d, e) show an overall good agreement with two independent experimental datasets[25,26] in the 0-1 bar region, and Supplementary Figs. 54 and 55 (273–313 K) further confirming the reliability of our MLP to capture the CO_2 adsorption behavior in the overall range of investigated temperature range. The MLP-MD derived Radial Distribution Functions (RDFs) computed for the predominant MOF/CO_2 atom pair at a given CO_2 loading of 2.02 mmol g^{-1} and 300 K is in very good agreement with that obtained by AIMD in the same conditions (Fig. 4f). This comparison supports that the MLP captures well μ_2-OH position and orientation changes upon CO_2 adsorption. As shown in Fig. 4g, h, Supplementary Figs. 56–58 and Supplementary Movies 1–4, the μ_2-OH groups in the MIL-120(Al)-F model undergo pronounced rotations on ps time scales in the MLP-MD-derived trajectories at 300 K, and this behavior appears both in the presence and absence of CO_2. At a low CO_2 loading of 2.02 mmol g^{-1}, analysis of the MLP-MD trajectories show that MIL-120(Al)-F structure reaches equilibrium after ~ 200 ps. The same structure loaded by 4.05 mmol g^{-1} of CO_2 attains an equilibrium faster (~ 95 ps). This indicates that the phase/ordering transition depends on the guest loading: a critical CO_2 density promotes cooperative reorientation and shortens the transition time. This interpretation is consistent with the relatively low CI-NEB energy barriers, which place μ_2-OH rotations within the range of thermal accessibility and allow guest-driven kinetics to control the observed timescales. Further examination of the adsorbate orientation indicates that the majority of the molecules are predominantly aligned in orientations axial to the channel, analogous to the low-energy structures of CO_2@MIL-120(Al)-C and CO_2@MIL-120(Al)-D (Fig. 4a). These findings reveal a complex interplay between the intrinsic conformational energetics of the MOF framework, governed by the local μ_2-OH dynamics, and the stabilization energy provided by the host-guest interactions. Notably in the case of the GCMC-(NVT) MD simulations (Supplementary Fig. 59), there is an overall reduction in CO_2 sorption uptake compared to the GCMC simulations, a phenomenon attributed to the local dynamics of the μ_2-OH groups. Nevertheless, the overall trend in sorption uptakes from MIL-120(Al)-F to MIL-120(Al)-A is preserved, particularly at higher pressures. This suggests that even with the dominance of the local μ_2-OH dynamics, the global relaxation of the MOF structure is required to accurately capture the overall adsorption phenomena.

Discussions

In summary, the combination of DFT calculations with a purpose-trained MLP, demonstrates that MIL-120(Al) can adopt a large set of configurations associated with distinct local μ_2-OH orientations. It was found that the commonly adopted structure model in the literature [MIL-120(Al)-F], in which the bridging μ_2-OH groups are pointing towards pore, is predicted to be a high-energy form in the empty scenario, whereas the MIL-120(Al)-A is the more stable configuration with its μ_2-OH groups arranged to form a cooperative, interlocking hydrogen-bond network. Notably, the energy barriers corresponding to the interconversion of these different structures are relatively small. Phonon calculations showed that all configurations are dynamically stable, and mechanical analysis revealed exceptional ductility along the AlO_6 octahedra chain direction. The so-developed MLP trained on an extensive DFT dataset reproduces DFT energetics, CI-NEB energy barriers and phonons for the empty structures, and beyond accurately predicts CO_2 adsorption geometries and energies within 2.3 kJ mol^{-1} of DFT values. We found that CO_2 does not significantly increase reorientation energy barriers and can even stabilize specific transition states, while conversely μ_2-OH orientation controls whether CO_2 binds parallel or perpendicular to the channel and thereby tunes adsorption energetics. Indeed, these computational findings evidence that the local dynamics of the μ_2-OH groups play a major role in the CO_2 location and energetics in this ultra-small pore MOF, a feature most often neglected using generic force fields and rigid MOF framework assumption. The precise location of the H atom that cannot be achieved by conventional X-ray diffraction techniques, combined with the flexibility of the μ_2-OH groups, is shown to control the pore aperture size and hence the CO_2 adsorption geometries and energetics. Furthermore, our MLP-based GCMC–MD strategy was demonstrated to be reliable for capturing accurately the host–guest interactions coupled with local structural dynamics, which cannot be achieved by applying a rigid framework UFF-based GCMC approach. More generally, these results also emphasize the necessity of system-specific, high-quality MLP for reliable predicting of the adsorption behaviors of guest molecules in ultra-small pore MOFs.

Methods

DFT calculations

All DFT calculations were carried out using the Vienna Ab-initio Simulation Package (VASP) code (Version: 5.4.4)[39]. The projector augmented wave (PAW) potential and the Perdew-Burke-Ernzerhof (PBE) exchange-correlation functional was adopted[40,41]. An energy cutoff of 650 eV and the Monkhorst-Pack 5 × 5 × 6 k-point grid[42] was chosen to ensure convergence of total energy. These parameters yielded converged total energies and atomic forces within thresholds of 10^{-5} eV and 0.01 eV $Å^{-1}$, respectively. All geometry optimizations were performed using the VASP code with the conjugate gradient (CG) algorithm. Dispersion interactions were accounted for using the DFT-D3 van der Waals (vdW) correction scheme[43]. The elastic constants were calculated using DFT-based static stress-strain calculations in VASP, where both lattice parameters and atomic positions were fully relaxed under small deformations to obtain the elastic tensor directly from

energy-minimized structures. Finite-temperature AIMD simulations were carried out in 2 × 2 × 2 supercells to better capture local dynamics and hydrogen-bond rearrangements. AIMD runs used the canonical (*NVT*) ensemble with a Nosé–Hoover thermostat and a time step of 0.5 fs[44]. The AIMD trajectories were collected at 300, 500 and 800 K for durations exceeding 5 ps. Symmetry constraints were removed in all AIMD simulations to allow unrestricted sampling of local reorientation modes. CI-NEB[27] calculations for transition-state pathways were performed within VASP using standard settings described in Supplementary Note 1.

Dataset preparation for MLP training

To build a representative training dataset for the MIL-120(Al)s family, we combined configurations from multiple sampling protocols: DFT geometry optimizations, static single-point calculations, random Widom-insertions of CO_2 at various loadings, structure optimizations under different strains and pressures, CI-NEB intermediate images sampled along μ_2-OH reorientation paths, and AIMD snapshots from both NVT and NPT ensembles. The dataset includes both empty and CO_2-loaded MIL-120(Al) configurations in unit-cell and supercell representations. In total 183,061 snapshots were collected. Further details are provided in Supplementary Notes 1 and 2.

MLP development

We trained a deep neural network potential using the DeePMD-kit (v2.0.1) implementation of the DeepPot-SE framework[28]. The embedding network sizes were set to {25, 50, 100} for successive embedding layers, while the fitting network used three hidden layers of sizes {240, 240, 240}. A radial cutoff of 7.8 Å and a smoothing-length of 1.2 Å were adopted to capture sufficient many-body information while maintaining computational efficiency for the MIL-120(Al)s environments. Training proceeded for 1,000,000 steps with an initial learning rate of 1×10^{-3} that decayed every 5000 steps; other hyperparameters (batching and loss weightings) follow the protocol summarized in Supplementary Note 2. The choice of cutoff and network depth was validated by convergence tests to ensure robust reproduction of DFT energies and forces for both empty and CO_2-loaded configurations.

MLP-based molecular dynamics and property calculations

The trained DeePMD potential was also deployed for large-scale molecular dynamics via the DeepMD-LAMMPS interface, using the model as a LAMMPS pair style for energy and force evaluations[45]. Phonon calculations were performed using Phonopy and the phono-LAMMPS toolchain on 2 × 2 × 2 supercells along a consistent Brillouin zone path[46,47]. CI-NEB pathways were recomputed using the ASE-Python library[48] and the trained MLP, with each intermediate structure optimized using the FIRE (Fast Inertial Relaxation Engine) algorithm, enabling extensive transition-state sampling at lower computational cost. The MLP was also used for exhaustive CO_2 adsorption site discovery via Widom-insertion sampling and adsorption energy scans.

MLP-based hybrid GCMC simulations

To incorporate the framework dynamics and simulations with the trained MLP, we developed custom code to perform GCMC simulations based on MLP energies. The code performs insertion, deletion, rotation, and translation moves on the adsorbed molecule based on the Metropolis algorithm[49], with acceptance criteria calculated according to

$$P_{\mathrm{INSERTION}}(O \to N) = \min\left\{1, \frac{\beta f V}{N+1}\exp(-\beta\Delta U)\right\} \quad (1)$$

$$P_{\mathrm{DELETION}}(O \to N) = \min\left\{1, \frac{N}{\beta f V}\exp(-\beta\Delta U)\right\} \quad (2)$$

$$P_{\mathrm{ROTATION}}(O \to N) = \min\left\{1, \exp(-\beta\Delta U)\right\} \quad (3)$$

$$P_{\mathrm{TRANSLATION}}(O \to N) = \min\left\{1, \exp(-\beta\Delta U)\right\} \quad (4)$$

where β is the reciprocal thermodynamic temperature, $1/k_BT$, with k_B being the Boltzmann constant, U represents the potential energy of interaction, N the number of adsorbate molecules in the simulation box, V the volume of the simulation box, and f the fugacity of the adsorbing species. The fugacity was calculated as $f = \phi P$, with P being the pressure on the ideal reservoir and ϕ the fugacity coefficient, calculated by the Peng-Robinson equation of state[50].

The code is based on the ASE-Python library[48], with the energy evaluations being performed by the DeePMD-ASE calculator interface. The molecular dynamics (MD) simulations on the NVT ensemble were performed with the Berendsen thermostat, and on the NPT ensemble with the Berendsen thermostat and barostat[51]. For all simulations, a quasi-cubic unit cell with cell parameters larger than 25 Å was created.

To sample the configurational space at each point, we implemented a hybrid MD + GCMC protocol consisting of ten primary cycles. Each cycle was partitioned in 20,000 GCMC steps followed by 20,000 MD steps with a time step of 0.5 fs. Convergence was further refined through an additional 500,000 GCMC steps to obtain the equilibrated averages. Statistical analysis of the equilibrated averages was performed using pyMSER[52].

Data availability

The data used in this study are available in the Zenodo database in ref. 53. Source data are provided with this paper.

Code availability

The primary packages utilized in this article include VASP (https://www.vasp.at) and DeePMD-kit (https://github.com/deepmodeling/deepmd-kit). The adsorption code can be accessed online at https://github.com/lipelopesoliveira/flames. Detailed information about the license and the user manual can be found in the abovementioned articles and on their websites.

References

1. Furukawa, H., Cordova, K. E., O'Keeffe, M. & Yaghi, O. M. The chemistry and applications of metal-organic frameworks. *Science* **341**, 1230444 (2013).
2. Zhou, H. C. J. & Kitagawa, S. Metal–organic frameworks (MOFs). *Chem. Soc. Rev.* **43**, 5415–5418 (2014).
3. Férey, G. Hybrid porous solids: past, present, future. *Chem. Soc. Rev.* **37**, 191–214 (2008).
4. Cheng, Y. et al. Advances in metal–organic framework-based membranes. *Chem. Soc. Rev.* **51**, 8300–8350 (2022).
5. Demir, H., Daglar, H., Gulbalkan, H. C., Aksu, G. O. & Keskin, S. Recent advances in computational modeling of MOFs: from molecular simulations to machine learning. *Coord. Chem. Rev.* **484**, 215112 (2023).
6. Formalik, F., Shi, K., Joodaki, F., Wang, X. & Snurr, R. Q. Exploring the structural, dynamic, and functional properties of metal-organic frameworks through molecular modeling. *Adv. Funct. Mater.* **34**, 2308130 (2024).
7. Rohde, R. C. et al. High-temperature carbon dioxide capture in a porous material with terminal zinc hydride sites. *Science* **386**, 814–819 (2024).
8. McDonald, T. M. et al. Capture of carbon dioxide from air and flue gas in the alkylamine-appended metal–organic framework mmen-Mg_2(dobpdc). *J. Am. Chem. Soc.* **134**, 7056–7065 (2012).
9. Liu, T. et al. Bottom-up computational design of shape-selective organic macrocycles for humid CO_2 capture. *Nat. Chem.* **17**, 1696–1704 (2025).

10. Lin, J.-B. et al. A scalable metal-organic framework as a durable physisorbent for carbon dioxide capture. *Science* **374**, 1464–1469 (2021).
11. Ye, Z.-M. et al. Architecting metal–organic frameworks at molecular level toward direct air capture. *J. Am. Chem. Soc.* **147**, 5495–5514 (2025).
12. Van Speybroeck, V. & Maurin, G. Materials for a changing planet. *Nat. Mater.* **22**, 12–13 (2023).
13. Adil, K. et al. Gas/vapour separation using ultra-microporous metal–organic frameworks: insights into the structure/separation relationship. *Chem. Soc. Rev.* **46**, 3402–3430 (2017).
14. Wang, J. et al. Fine pore engineering in a series of isoreticular metal-organic frameworks for efficient C_2H_2/CO_2 separation. *Nat. Commun.* **13**, 200 (2022).
15. Senkovska, I., Bon, V., Mosberger, A., Wang, Y. & Kaskel, S. Adsorption and separation by flexible MOFs. *Adv. Mater.* **37**, 2414724 (2025).
16. Zhang, Z., Yao, Z.-Z., Xiang, S. & Chen, B. Perspective of microporous metal–organic frameworks for CO_2 capture and separation. *Energy Environ. Sci.* **7**, 2868 (2014).
17. Trickett, C. A. et al. The chemistry of metal–organic frameworks for CO_2 capture, regeneration and conversion. *Nat. Rev. Mater.* **2**, 17045 (2017).
18. Cadiau, A. et al. Hydrolytically stable fluorinated metal-organic frameworks for energy-efficient dehydration. *Science* **356**, 731–735 (2017).
19. Ebadi Amooghin, A., Sanaeepur, H., Luque, R., Garcia, H. & Chen, B. Fluorinated metal–organic frameworks for gas separation. *Chem. Soc. Rev.* **51**, 7427–7508 (2022).
20. Bhatt, P. M. et al. A fine-tuned fluorinated MOF addresses the needs for trace CO_2 removal and air capture using physisorption. *J. Am. Chem. Soc.* **138**, 9301–9307 (2016).
21. Chen, X. et al. Flexibility-frustrated porosity for enhanced selective CO_2 adsorption in an ultramicroporous metal-organic framework. *Chem.* **11**, 102382 (2025).
22. Yao, X., Cordova, K. E. & Zhang, Y.-B. Flexible metal–organic frameworks as CO_2 adsorbents en route to energy-efficient carbon capture. *Small Struct.* **3**, 2100209 (2022).
23. Chung, Y. G. et al. Advances, updates, and analytics for the computation-ready, experimental metal–organic framework database: CoRE MOF 2019. *J. Chem. Eng. Data* **64**, 5985–5998 (2019).
24. Volkringer, C. et al. Occurrence of uncommon infinite chains consisting of edge-sharing octahedra in a porous metal organic framework-type aluminum pyromellitate $Al_4(OH)_8[C_{10}O_8H_2]$ (MIL-120): synthesis, structure, and gas sorption properties. *Chem. Mater.* **21**, 5783–5791 (2009).
25. Chen, B. et al. A scalable robust microporous Al-MOF for post-combustion carbon capture. *Adv. Sci.* **11**, 2401070 (2024).
26. Loughran, R. P. et al. CO_2 capture from wet flue gas using a water-stable and cost-effective metal-organic framework. *Cell Rep. Phys. Sci.* **4**, 101470 (2023).
27. Henkelman, G., Uberuaga, B. P. & Jónsson, H. A climbing image nudged elastic band method for finding saddle points and minimum energy paths. *J. Chem. Phys.* **113**, 9901–9904 (2000).
28. Wang, H., Zhang, L., Han, J. & E, W. DeePMD-kit: a deep learning package for many-body potential energy representation and molecular dynamics. *Comput. Phys. Commun.* **228**, 178–184 (2018).
29. Gu, Q. et al. Deep learning tight-binding approach for large-scale electronic simulations at finite temperatures with ab initio accuracy. *Nat. Commun.* **15**, 6772 (2024).
30. Morrow, J. D., Gardner, J. L. A. & Deringer, V. L. How to validate machine-learned interatomic potentials. *J. Chem. Phys.* **158**, 121501 (2023).
31. Henkelman, G. & Jónsson, H. Improved tangent estimate in the nudged elastic band method for finding minimum energy paths and saddle points. *J. Chem. Phys.* **113**, 9978–9985 (2000).
32. Batatia, I. et al. A foundation model for atomistic materials chemistry. *J. Chem. Phys.* **163**, 184110 (2025).
33. Lim, Y., Park, H., Walsh, A. & Kim, J. Accelerating CO_2 direct air capture screening for metal-organic frameworks with a transferable machine learning force field. *Matter* **8**, 102203 (2025).
34. Kaplan, A. D. et al. A foundational potential energy surface dataset for materials. Preprint at https://arxiv.org/abs/2503.04070 (2025).
35. Wood, B. M. et al. UMA: a family of universal models for atoms. Preprint at https://arxiv.org/abs/2506.23971 (2025).
36. Rappe, A. K., Casewit, C. J., Colwell, K. S., Goddard, W. A. & Skiff, W. M. UFF, a full periodic table force field for molecular mechanics and molecular dynamics simulations. *J. Am. Chem. Soc.* **114**, 10024–10035 (1992).
37. Boyd, P. G. et al. Data-driven design of metal–organic frameworks for wet flue gas CO_2 capture. *Nature* **576**, 253–256 (2019).
38. Li, Y., Jin, X., Moubarak, E. & Smit, B. A refined set of universal force field parameters for some metal nodes in metal–organic frameworks. *J. Chem. Theory Comput.* **20**, 10540–10552 (2024).
39. Kresse, G. & Furthmüller, J. Efficient iterative schemes for ab initio total-energy calculations using a plane-wave basis set. *Phys. Rev. B* **54**, 11169–11186 (1996).
40. Blöchl, P. E. Projector augmented-wave method. *Phys. Rev. B* **50**, 17953–17979 (1994).
41. Perdew, J. P., Burke, K. & Ernzerhof, M. Generalized gradient approximation made simple. *Phys. Rev. Lett.* **77**, 3865–3868 (1996).
42. Monkhorst, H. J. & Pack, J. D. Special points for Brillouin-zone integrations. *Phys. Rev. B* **13**, 5188–5192 (1976).
43. Grimme, S. Semiempirical GGA-type density functional constructed with a long-range dispersion correction. *J. Comput. Chem.* **27**, 1787–1799 (2006).
44. Nosé, S. A molecular dynamics method for simulations in the canonical ensemble. *Mol. Phys.* **52**, 255–268 (1984).
45. Thompson, A. P. et al. LAMMPS—a flexible simulation tool for particle-based materials modeling at the atomic, meso, and continuum scales. *Comput. Phys. Commun.* **271**, 108171 (2022).
46. Togo, A., Chaput, L., Tadano, T. & Tanaka, I. Implementation strategies in phonopy and phono3py. *J. Phys. Condens. Matter* **35**, 353001 (2023).
47. Carreras, A. phonoLAMMPS: a python interface for LAMMPS phonon calculations using phonopy. *Zenodo* https://doi.org/10.5281/zenodo.3940626 (2020).
48. Hjorth Larsen, A. et al. The atomic simulation environment—a Python library for working with atoms. *J. Phys. Condens. Matter* **29**, 273002 (2017).
49. Metropolis, N., Rosenbluth, A. W., Rosenbluth, M. N., Teller, A. H. & Teller, E. Equation of state calculations by fast computing machines. *J. Chem. Phys.* **21**, 1087–1092 (1953).
50. Peng, D.-Y. & Robinson, D. B. A new two-constant equation of state. *Ind. Eng. Chem. Fund.* **15**, 59–64 (1976).
51. Berendsen, H. J. C., Postma, J. P. M., Van Gunsteren, W. F., DiNola, A. & Haak, J. R. Molecular dynamics with coupling to an external bath. *J. Chem. Phys.* **81**, 3684–3690 (1984).
52. Oliveira, F. L., Luan, B., Esteves, P. M., Steiner, M. & Neumann Barros Ferreira, R. pyMSER—an open-source library for automatic equilibration detection in molecular simulations. *J. Chem. Theory Comput.* **20**, 8559–8568 (2024).
53. Fan, D., Oliveira, F. L., Bonakala, S., Wahiduzzaman, M. & Maurin, G. Decoding local framework dynamics in the ultra-small pore MOF MIL-120(Al) CO_2 sorbent with machine-learning potential. Zenodo database. https://doi.org/10.5281/zenodo.17618381 (2025).

Acknowledgements

The computational work was performed using HPC resources from GENCI-CINES (Grant No. A0180907613; G.M.). This work was also partly supported by the Natural Science Foundation of China (Grant No.

22503009; D.F.) and the Science and Technology Research Program of Chongqing Municipal Education Commission (Grant No. KJQN202500748; D.F.). G.M. thanks the Institut Universitaire de France for the Senior Chair. We thank G. Mouchaham (IMAP, ESPCI, ENS, CNRS) for insightful discussions on the experimental CO_2 adsorption data.

Author contributions

D.F. and G.M. designed the research. D.F., F.O., S.B., and M.W. carried out the simulations. D.F., F.O., S.B., M.W., and G.M. wrote the manuscript. G.M. supervised and guided the research.

Competing interests

The authors declare no competing interests.

Additional information

Supplementary information The online version contains supplementary material available at https://doi.org/10.1038/s41467-026-69993-x.

Correspondence and requests for materials should be addressed to Guillaume Maurin.

Peer review information *Nature Communications* thanks Renjith Pillai and the other, anonymous, reviewer(s) for their contribution to the peer review of this work. A peer review file is available.